Communications in Computational Chemistry
Commun. Comput. Chem., Vol. 7, No. 1, 42–49
doi: 10.4208/cicc.2025.62.01
Regular Article

Mechanism for the Inhibition of Dewetting in Polymer Thin Films by Interface Segregation of Single-Chain Nanoparticles

Zhao Qian[1,3], Rui Shi [1,*], Zhongyuan Lu[1] and Hujun Qian[1, 2,*]

[1] *State Key Laboratory of Supramolecular Structure and Materials, Institute of Theoretical Chemistry, College of Chemistry, Jilin University, Changchun 130012, China;*

[2] *Key Laboratory of Material Simulation Methods & Software of Ministry of Education*, *Jilin University, Changchun 130012, China;*

[3] *National Engineering Research Center for Rare Earth, Grirem Advanced Materials Co.,Ltd, Beijing 100088, China.*

[*] Corresponding authors: shirui816@jlu.edu.cn, hjqian@jlu.edu.cn

Received on 03 March 2025; Accepted on 05 April 2025

Abstract: The inhibition of dewetting in polymer thin films (PTFs) is crucial for their practical applications. Through molecular dynamics simulations, we elucidate the mechanism of interface segregation of single-chain nanoparticles (SCNPs) in inhibiting PTF dewetting. Our study provides atomic-level insights into three key aspects: (1) how SCNP segregation affects the contact angle, (2) how it influences the orientation of matrix chains at the interface, and (3) how the interaction between solvent molecules and cross-linkers within SCNPs influences the dewetting behavior. By employing static droplet and dynamic pre-punched film models, we systematically investigate the effects of SCNP doping concentration and cross-linker-solvent interaction strength. Our results demonstrate that SCNP segregation significantly alters the orientation of linear polymer chains at the interface. In pure polymer films, chain ends preferentially accumulate at the interface due to entropic effects, leading to parallel chain conformations. However, SCNP segregation suppresses this effect, promoting more vertical chain orientations. Furthermore, we find that weaker cross-linker-solvent interactions promote SCNP segregation at the substrate interface, leading to more effective dewetting inhibition. These findings provide fundamental understanding and practical guidance for designing stable polymer thin films through nanoparticle doping.

Key words: polymer thin films, single-chain nanoparticle, dewetting inhibition.

1. Introduction

Polymer thin films (PTFs) on solid substrates have become indispensable in various technological applications, ranging from protective coatings to optoelectronic devices [1-9]. A fundamental challenge in these applications is maintaining film stability and preventing dewetting, particularly for thin films where molecular forces dominate [10-12]. Recent experimental studies have highlighted the potential of nanoparticle doping as an effective strategy for dewetting inhibition [13-22]. Among various nanoparticles, single-chain nanoparticles (SCNPs) have shown particular promise due to their unique structure and compatibility with polymer matrices.[17] However, while experimental observations

have established the correlation between SCNP interface segregation and dewetting inhibition, the underlying atomic-level mechanisms remain poorly understood.

Here, by performing comprehensive molecular dynamics simulation, we address this knowledge gap by providing detailed insights into three crucial aspects of SCNP-induced dewetting inhibition. First, we elucidate how SCNP segregation at the interface affects the macroscopic contact angle. Second, we reveal a significant effect on the microscopic orientation of matrix polymer chains. In pure polymer films, chain ends preferentially accumulate at the interface due to entropic effects, resulting in parallel chain conformations. However, SCNP segregation dramatically alters this behavior, promoting more vertical chain orientations at the interface. Third, we investigate the often-overlooked but critical role of solvent/cross-linker interactions in the dewetting process. Specifically, we examine how the interaction strength between solvent molecules and cross-linkers within SCNPs influences the segregation behavior and subsequent dewetting inhibition.

Building upon our previous simulation studies [23,24], as shown in Figure 1, we employ all-polymer nanocomposite films doped with SCNPs, where the chemical similarity between SCNP monomers and polymer matrix components allows us to isolate and examine the specific effects of cross-linker-solvent interactions. Our simulation results reveal that weaker cross-linker-solvent interactions promote more effective SCNP segregation at the substrate interface, leading to enhanced dewetting inhibition. These findings not only provide fundamental understanding of the dewetting inhibition mechanism but also offer practical guidance for optimizing nanoparticle-doped polymer thin films through careful control of solvent-cross-linker interactions and manipulation of chain orientations at interfaces.

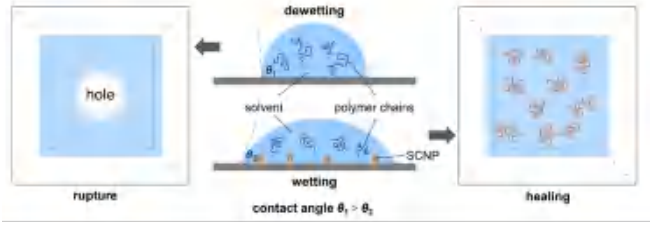

Figure 1. Schematic diagram of polymer film dewetting inhibition by interface segregation of SCNPs.

2. Methods

2.1 Models and parameters

To comprehensively investigate the inhibition effect of segregated single-chain nanoparticles (SCNPs) on polymer chain dewetting, we employ both static (droplet) and dynamic (pre-punched thin film) systems. The static droplet system allows for contact angle measurement to assess wettability, while the dynamic pre-punched film system enables monitoring of hole area evolution as an indicator of dewetting behavior.

Both systems consist of the following components: substrate, linear polymer chains, SCNPs, and solvent. We employ the Kremer-Grest model [25] to simulate polymer chains and SCNPs. With non-bonded interactions described by the Lennard-Jones potential::

$$U(r) = \begin{cases} 4\varepsilon\left[\left(\frac{\sigma}{r}\right)^{12} - \left(\frac{\sigma}{r}\right)^{6}\right] & \text{for } r < r_c \\ 0 & \text{for } r \geq r_c \end{cases} \quad (1)$$

where ε, σ and r_c are the interaction strength, bead size and truncated interaction range respectively. The finitely extensible nonlinear elastic potential is used to describe the bonds in both polymer chains and SCNPs,

$$U(r) = -\frac{1}{2}kr_m^2 \log\left[1 - \frac{(r)^2}{r_m^2}\right] + \left\{4\varepsilon\left[\left(\frac{\sigma}{r}\right)^{12} - \left(\frac{\sigma}{r}\right)^{6}\right] + \varepsilon\right\} \quad (2)$$

in which k, r_m are attractive force strength and maximum bond length, respectively. The second Lennard-Jones term is used to avoid overlapping between bonding pairs, and it is truncated at a cutoff distance of $2^{1/6}\sigma$. All simulations are performed with reduced units, with the energy, the bead diameter, and the bead mass set as $\varepsilon_0 = \sigma_0 = m_0 = 1$. Therefore, the time has a unit of $\tau_0 = \sqrt{m\sigma_0^2/\varepsilon_0}$. In our simulation, r_c is fixed at $2.5\,\sigma_0$. For bond potential, k is fixed at $30\,\varepsilon_0/{\sigma_0}^2$, $r_m = 1.5\,\sigma_0$ and r_0 =1.0 σ_0. Interaction strength parameter ε used in our simulation between different components are listed in Table 1.

The values of ε between the different components are determined by the modified Lorentz-Berthelot combination rule [26-28], i.e., $\varepsilon_{ij} = \lambda_{ij}\sqrt{\varepsilon_{ii}\,\varepsilon_{jj}}$. Here, λ is a tunable parameter, typically ranging from 0.2 to 2 [28]. In our simulations, we select values for λ_{SX} within the range [0.5, 1.5], which corresponds to an effective Flory χ approximately spanning from –3 to 3. This interval covers conditions from very good to poor solubility, allowing for reasonable extrapolation of the behavior. All the simulations are performed under *NVT* condition with a time step of $dt = 0.005\,\tau_0$, Nosé-Hoover thermostat is used to control the temperature. All simulations in this work are performed with the GALAMOST package [29].

Table 1. Interaction strength between different bead types in the system.

E	**P**	**X**	**S**	**W**
P	1.0	1.0	1.5	0.5
X		1.0	0.5~1.5[a]	1.5
S			1.0	0.5
W				

[a] The specific values of ε_{SX} are shown in the following simulations. Here P, X, S, W stand for matrix linear polymer monomers, cross-linkers in SCNP, solvent, and wall particles, respectively.

2.2 Contact angle calculation algorithm

Building upon the work of Liu and Zhang et al., [30] we implement the Quickhull algorithm [31] determine the contact angle between polymer droplets and substrates. Unlike previous studies, our system primarily consists of polymer chains and SCNPs, enabling direct extraction of the droplet profile from their coordinates without considering residual solvent effects.

The Quickhull algorithm efficiently processes three-dimensional data points, generating a convex hull composed of triangular facets that encompass all data points. As illustrated in Figure 2, this approach produces an irregular convex polygon bounded by triangles, facilitating accurate contact angle determination through vector analysis. Key advantages of the Quickhull algorithm include: (i) computational efficiency; (ii) robustness against numerical imprecision (round-off errors in floating-point arithmetic); (iii) direct integration with Scipy library. For each triangular facet, we define three vectors ($\mathbf{v}_1$, $\mathbf{v}_2$, and $\mathbf{v}_3$) from the origin and calculate the normal vector: $\mathbf{n} = (\mathbf{v}_1 - \mathbf{v}_2) \times (\mathbf{v}_1 - \mathbf{v}_3)$, where $\mathbf{n} = n_1\mathbf{i} + n_2\mathbf{j} + n_3\mathbf{k}$ represents the normal vector, and **i**, **j**, and **k** are the unit vectors in the *X*, *Y*, and *Z* directions, respectively. The contact angle is then calculated as:

$$\theta = \cos^{-1}\left(\frac{n_3}{\sqrt{(n_1^2 + n_2^2 + n_3^2)}}\right) \quad (3)$$

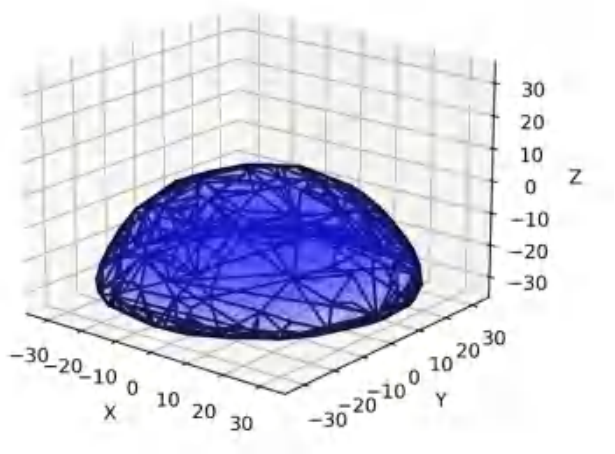

Figure 2. Convex hull of polymer nanocomposite droplet constructed using the Quickhull algorithm. Blue dots represent monomeric particles of polymer chains and SCNPs; black triangles indicate peripheral contours.

2.3 Calculation of the hole area

The hole area in pre-punched thin films serves as a quantitative measure of dewetting, representing the exposed substrate area not covered by polymer chains or SCNPs. Complete wetting corresponds to zero hole area, while increasing hole size indicates more severe dewetting. As illustrated in Figure 3a, the initial configuration features a central uncovered region.

To quantify the hole area, we implement the following procedure:

1. Divide the simulation box into a 120×120 grid in the XY plane
2. Calculate the density distribution of polymer chains and SCNPs at each lattice site
3. Generate a density map (Figure 3b)
4. Determine the hole area by counting zero-density lattice points

This method provides a robust and efficient approach to monitor dewetting dynamics through hole area evolution.

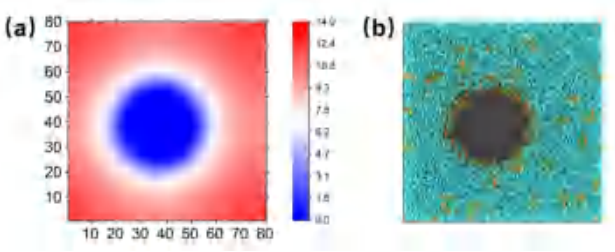

Figure 3. (a) Initial configuration showing the central uncovered region in the pre-punched film. (b) Two-dimensional density distribution of solute components in the XY plane.

3. Results

3.1 Pure Polyumer systems

We first examine the wettability of pure polymers on non-infiltrated substrates. Figure 4 presents equilibrium conformations of both pure polymers melt droplets and semi-dried droplets containing 20% solvent. Visual inspection of these snapshots reveals contact angles ≥90° for both systems, indicating poor wettability.

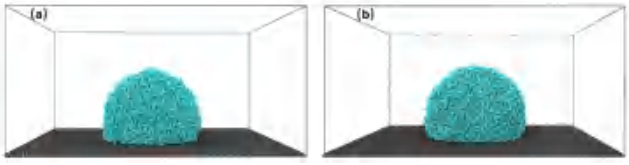

Figure 4. Equilibrium morphologies of (a) pure polymer melt droplets and (b) semi-dried droplets containing 20% solvent.

To further investigate dewetting behavior, we simulate pre-punched thin films, with results shown in Figure 5 The initial configuration (similar to Figure 3b) features a central hole with radius 5σ and area ≈80σ². Upon simulation, rapid hole expansion leads to complete film rupture and droplet formation within a short timescale. The morphological evolution of this process is detailed in Figure S1 in supporting information.

Key observations from these simulations include:

1. Significant dewetting occurs on non-infiltrated surfaces
2. Both melt and semi-dried systems exhibit similar dewetting behavior
3. Rapid hole expansion precedes film rupture
4. Final state consists of isolated droplets

These results underscore the importance of dewetting inhibition,

particularly given the mechanical instability of dewetted films under external forces.

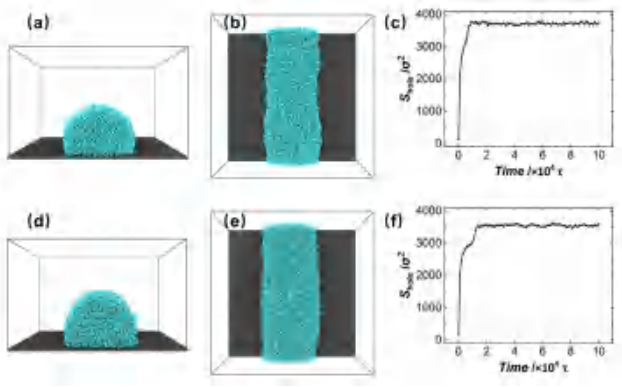

Figure 5. Dewetting dynamics of pre-punched films: (a-c) pure melt system; (d-f) semi-dried system (20% solvent). (a,d) Side views after rupture; (b,e) Top views after rupture; (c,f) Hole area evolution.

3.2 Effect of doping numbers of SCNPs

We systematically investigate the influence of SCNP concentration on dewetting inhibition in all-polymer nanocomposite (all-PNC) systems. The number of SCNPs is varied from 50 to 300 in increments of 50, with fixed interaction strengths ($\varepsilon_{WX} = 1.5, \varepsilon_{SX} = 0.5$). Figure 6 presents equilibrium morphologies of all-PNC droplets at different SCNP concentrations, revealing two key trends: (i) increased SCNP segregation at the substrate interface with higher doping levels and (ii) gradual decrease in contact angle, indicating improved wettability.

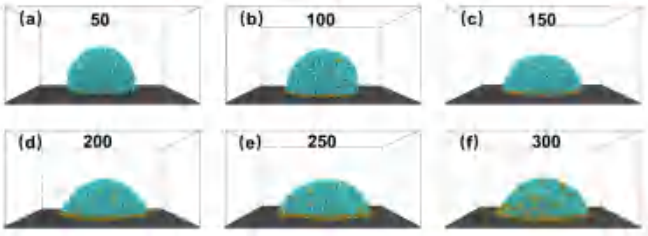

Figure 6. Side views of all-PNC droplets at equilibrium with varying SCNP numbers.

Results of quantitative analysis using the Quickhull algorithm are shown in Figure 7, it demonstrates a concentration-dependent dewetting inhibition: (i) below 100 SCNPs: Minimal contact angle reduction (limited dewetting inhibition); (ii) 100-250 SCNPs: Significant contact angle decrease (effective dewetting inhibition); (iii) above 250 SCNPs: Diminishing returns in contact angle reduction.

To further validate these findings, we examine hole evolution in pre-punched thin films with increased SCNP concentrations (200-400) to account for larger substrate contact areas. Figure 8 shows top-view snapshots after 2×10^5 τ simulations, demonstrating improved hole healing with higher SCNP concentrations.

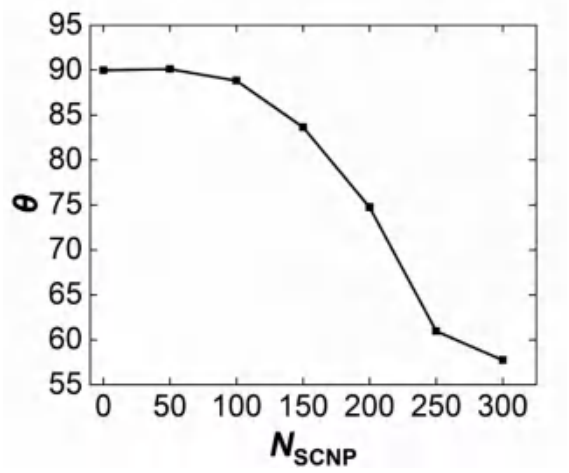

Figure 7. Contact angle versus SCNP number for all-PNC droplets.

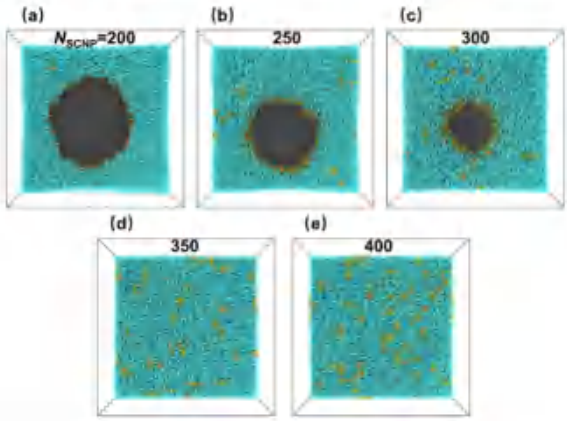

Figure 8. Top views of pre-punched films with varying SCNP numbers after 2×10^5 τ simulations.

Detailed hole area evolution analysis (Figure 9) reveals distinct behaviors: (i) 200-250 SCNPs: Rapid hole expansion followed by stabilization; (ii) 300 SCNPs: Initial expansion with subsequent shrinkage and complete healing; (iii) 350-400 SCNPs: Immediate hole healing upon constraint removal (inset). These results confirm that increased SCNP doping enhances dewetting inhibition, consistent with droplet system observations (Figs. 6-7).

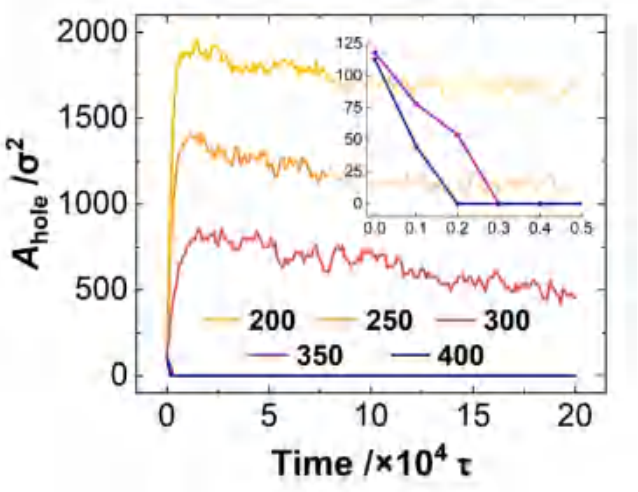

Figure 9. Hole area evolution over time for pre-punched films with varying SCNP numbers. Inset shows initial healing dynamics for 350-400 SCNPs.

3.3 Effect of solvent selectivitives

Building upon our previous findings regarding solvent selectivity effects on SCNP dispersion and interface segregation, we investigate how solvent selectivity influences polymer dewetting inhibition. The selectivity, quantified by the interaction strength ε_{SX} between solvent and cross-linkers, directly affects system interface tension and SCNP distribution.

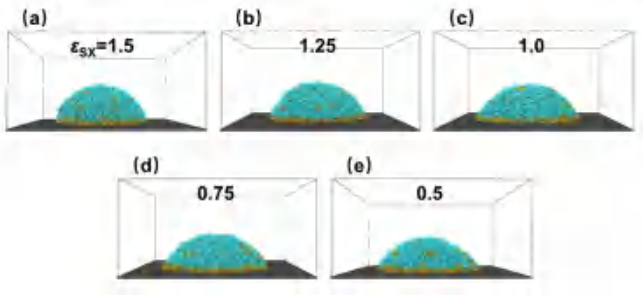

Figure 10. Side views of all-PNC droplets at equilibrium with varying ε_{SX}.

We perform simulations with fixed SCNP concentration (300) and substrate-cross-linker interaction strength (ε_{WX} = 1.5), while varying ε_{SX}. Figure 10 presents equilibrium morphologies of all-PNC droplets at different ε_{SX} values, revealing a clear trend: decreasing ε_{SX} (increasing solvent selectivity) leads to improved wettability, as evidenced by reduced contact angles shown in Figure 11. Quantitative analysis of contact angle values demonstrates that: (i) High ε_{WX} (low selectivity): Large contact angles, poor wettabilit;(ii) Intermediate ε_{WX}: Gradual contact angle reduction; (iii) Low ε_{WX} (high selectivity): Significant contact angle decrease, enhanced wettability. This behavior can be explained by two complementary mechanisms: (i) Enhanced SCNP segregation at the substrate interface with increasing solvent selectivity; (ii) Stronger affinity between cross-linkers and substrate promoting interface stabilization. These results demonstrate that solvent selectivity plays a crucial role in determining dewetting behavior, with higher selectivity leading to more effective dewetting inhibition through enhanced SCNP segregation.

To further investigate solvent selectivity effects, we simulate hole evolution in pre-punched films with fixed SCNP concentration (300) and solvent content (20%). Figure 12 presents top-view snapshots after 2×10^5 τ simulations following constraint removal, revealing important insights into film behavior. The initial central hole exhibits lateral displacement, though this movement is inconsequential due to periodic boundary conditions in the horizontal direction. More significantly, we observe a clear correlation between ε_{SX} and hole size. Films with high ε_{SX} (low selectivity) maintain larger holes, indicating poorer stability, while those with low ε_{SX} (high selectivity) show smaller or fully healed holes, reflecting enhanced stability. These results demonstrate that increased solvent selectivity, characterized by lower ε_{SX} values, promotes film stability through enhanced SCNP segregation at the substrate interface and more effective hole healing. The observed hole size trends provide consistent evidence for the crucial role of

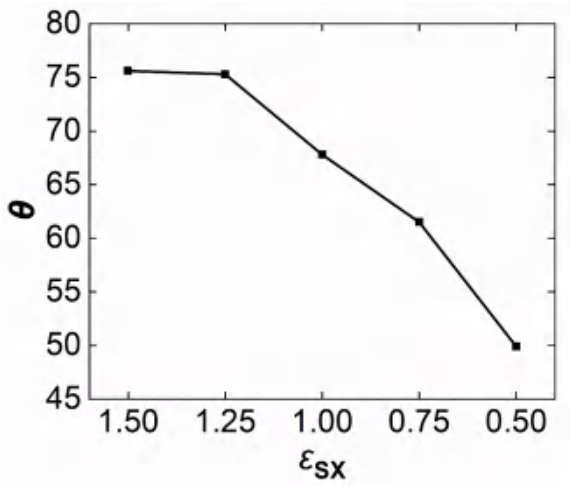

Figure 11. Contact angle versus ε_{SX} for all-PNC droplets.

solvent selectivity in controlling dewetting behavior, corroborating our findings from the droplet system studies. To better understand the temporal evolution of film hole structures, we analyze hole area changes during 2×10^5 τ simulations, results are shown in Figure 13a. Immediately following constraint removal, all systems exhibit rapid hole expansion, reflecting initial dewetting tendencies. Subsequent behavior varies significantly with ε_{SX} values. Systems with higher ε_{SX} (1.5, 1.25, 1.0) reach a stable plateau, maintaining relatively constant hole sizes. In contrast, systems with lower ε_{SX} (0.75, 0.5) show continued hole area reduction, particularly pronounced in the ε_{SX} = 0.5 system.

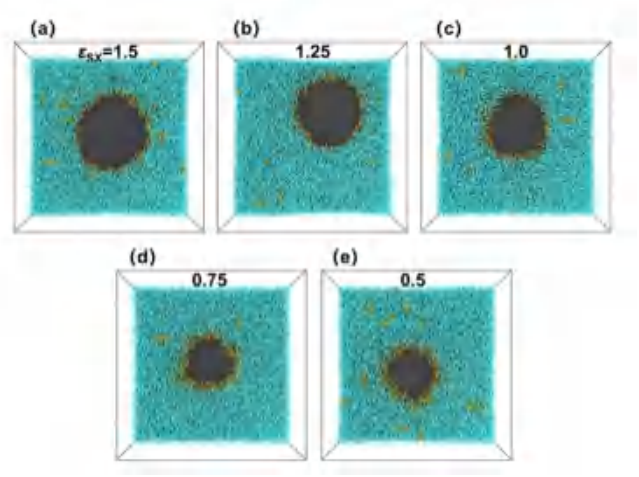

Figure 12. Top views of pre-punched films with varying ε_{SX} after 2×10^5 τ simulations.

To capture these dynamic processes more comprehensively, we extended simulations to 4×10^5 τ for the ε_{SX} = 0.75 and 0.5 systems (Figure 13b). The ε_{SX} = 0.75 system demonstrates gradual hole shrinkage, though complete healing is not achieved within the simulation timeframe. Notably, the ε_{SX} = 0.5 system achieves complete hole healing by 3×10^5 τ, highlighting the strong dewetting inhibition at high solvent selectivity.

These results demonstrate that solvent selectivity not only affects final hole sizes but also governs the kinetics of dewetting inhibition. The observed differences in healing rates and final states provide valuable insights for designing polymer films with controlled stability and self-healing properties.

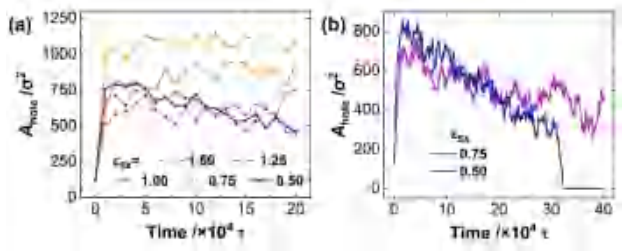

Figure 13. Hole area evolution over time for pre-punched films with varying ε_{SX}: (a) Initial 2×10^5 τ (sampled every 10000 τ); (b) Extended simulation to 4×10^5 τ for ε_{SX} = 0.75 and 0.5 (sampled every 1000 τ).

3.4 Mechanism of Dewetting Inhibition

To elucidate the mechanism behind SCNP-induced dewetting inhibition, we compare pure polymer films with all-PNC films containing 1000 polymer chains and 400 SCNPs. Both of the films contain 25% solvent molecules. Following system equilibration, we observe significant SCNP segregation at the substrate interface in all-PNC films.

We analyze the variations of the end-to-end vector components of polymer chains along the horizontal and vertical components of the film. The results are shown in Figure 14. Note that if the orientation of the polymer chains is isotropic, the end-to-end vectors along three directions are indistinguishable, i.e., $\langle R\rangle^X = \langle R\rangle^Y = \langle R\rangle^Z$. Herein, the horizontal direction component of the chain end-to-end distance $\langle R\rangle^{\parallel}$ is defined as

$$\sqrt{\frac{\left(\langle R\rangle^X\right)^2+\left(\langle R\rangle^Y\right)^2}{2}},$$

and the perpendicular direction component $\langle R\rangle^{\perp} = \langle R\rangle^Z$. From Figure 13 it can be seen that in most regions of the films, the $\langle R\rangle^{\parallel} \approx \langle R\rangle^{\perp}$, namely the polymer chains are basically isotropic. However, the difference of polymer chain conformation between the pure polymer film and all-PNC film only exists near the substrate. It can be seen that in the pure polymer film, the $\langle R\rangle^{\perp}$ is slightly smaller than $\langle R\rangle^{\parallel}$ near the substrate, while in the all-PNC film, $\langle R\rangle^{\perp}$ is significantly larger than $\langle R\rangle^{\parallel}$ near the substrate.

In addition, we analyze the density distribution of the free-end monomers (ρ_{End}) and the two middle monomers in the chain (ρ_{Middle}) along the *Z*-direction, and the results are shown in Figure 15. From which we see that for both films, the ρ_{End} is slightly higher than ρ_{Middle} in both substrate and vapor-liquid interface regions.

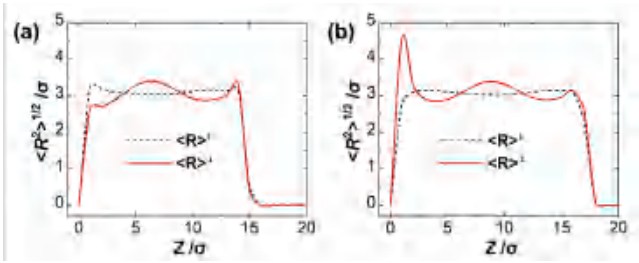

Figure 14. Horizontal ($\langle R\rangle^{\parallel}$) and vertical ($\langle R\rangle^{\perp}$ components of polymer chain end-to-end distance along the Z-direction in (a) pure polymer and (b) all-PNC films.

Especially in the substrate region for pure polymer film, while such density difference is highly restrained in all-PNC system with SCNPs presented, reducing the interfacial energy between the polymer film and the substrate.

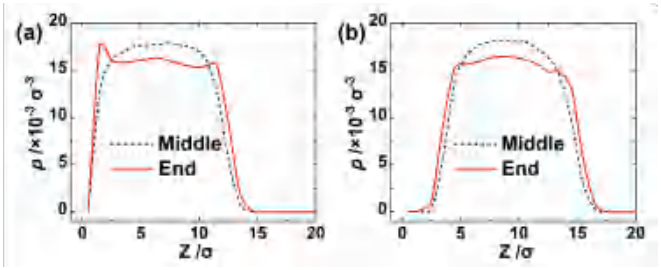

Figure 15. Density distribution of middle and end monomers along the Z-direction in (a) pure polymer and (b) all-PNC films.

These observations demonstrate that in pure polymer film, matrix chains tend to adopt parallel and relatively flat conformation due to the spatial constraints of the hard substrate. While in the PNC system, the space between SCNPs is filled by the free ends of matrix chains. Therefore, the matrix chains tend to adopt a perpendicular configuration. To further test this hypothesis, we analyze mean square displacement of matrix chains in the XY-direction (MSD_{XY}) across entire films, results are shown in Figure 16. It can be seen that the MSD_{XY} of polymer chains in the all-PNC film is indeed smaller than that in the pure film. The significantly reduced MSD_{XY} in all-PNC films confirms that SCNPs restrict lateral chain motion, thereby inhibiting dewetting. These findings provide fundamental insights into nanoparticle-mediated stabilization of polymer thin films, with implications for designing advanced coating materials with controlled stability.

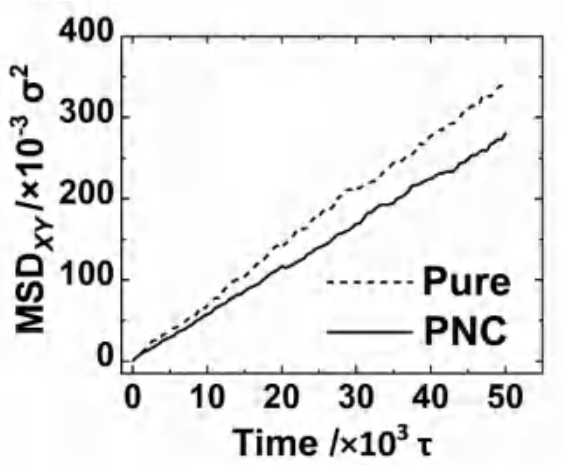

Figure 16. Mean square displacement in the XY-direction (MSD_{XY}) for polymer chains in pure polymer and all-PNC films.

4. Conclusions

Through comprehensive molecular dynamics simulations, we have elucidated the mechanisms by which interface segregation of single-

chain nanoparticles (SCNPs) inhibits dewetting in polymer thin films on non-infiltrated substrates. Our study employs both static droplet and dynamic pre-punched film models to provide a complete picture of polymer infiltration behavior.

Key findings from our investigation include: (i) Increased SCNP doping enhances dewetting inhibition, with optimal performance observed at higher concentrations where SCNPs effectively cover the substrate interface. (ii) Weaker interactions between solvent molecules and cross-linkers promote more effective SCNP segregation and dewetting inhibition. (iii) SCNPs inhibit dewetting through two primary mechanisms: it creates a porous interfacial structure that promotes vertical chain orientation, which physically restricting the lateral chain motion through chain penetration into SCNP networks.

Our findings demonstrate that the effectiveness of dewetting inhibition correlates strongly with the degree of SCNP segregation at the substrate interface. This fundamental understanding, supported by detailed analysis of polymer chain conformations and mean square displacement measurements, provides valuable insights for designing stable polymer thin films through nanoparticle doping. The mechanistic principles revealed in this study are not limited to the specific system investigated but are broadly applicable to various nanoparticle-doped polymer systems. These findings advance our understanding of nanoparticle-mediated stabilization in thin films and provide a foundation for developing advanced materials with controlled interfacial properties.

Supporting Information

The following supporting information can be downloaded at: https://global-sci.com/storage/self-storage/cicc-2025-62-1-r1-si.pdf.

Acknowledgments

This research is supported by the National Key Research and Development Program of China (2023YFB3812801) and by the National Natural Science Foundation of China (21873040, 22133002, and 21833008). Authors acknowledge the high-performance computing center of Jilin University. Hu-Jun Qian and Zhong-Yuan Lu also acknowledge the support from the Program for JLU Science and Technology Innovative Research Team.

References

[1] Harsányi, G. Polymer films in sensor applications: a review of present uses and future possibilities. *Sens. Rev.,* **20** (2) (2000), 98–105.

[2] Usui, H. Polymeric film deposition by ionization-assisted method for optical and optoelectronic applications. *Thin Solid Films,* **365** (1) (2000), 22–29.

[3] Gaur, P. K., Mishra, S., Gautam, R., et al. Film coating technology: past, present and future. *J. Pharm. Sci., Pharmacol,* **1** (1) (2014), 57–67.

[4] Harsányi, G. *Polymer Films in Sensor Applications*; Routledge, 1995. DOI: 10.1201/9780203742907.

[5] Yen, H.-J., Liou, G.-S. Design and preparation of triphenylamine-based polymeric materials towards emergent optoelectronic applications. *Prog. Polym. Sci.,* **89** (2019), 250–287.

[6] Yumashev, A., Mikhaylov, A. Development of polymer film coatings with high adhesion to steel alloys and high wear resistance. *Polym. Compos.,* **41** (7) (2020), 2875–2880.

[7] Mapari, S., Mestry, S., Mhaske, S. T. Developments in pressure-sensitive adhesives: a review. *Polym. Bull.* **78** (7) (2021), 4075–4108.

[8] Nam, S., Mooney, D. Polymeric tissue adhesives. *Chem. Rev.,* **121** (18) (2021), 11336–11384.

[9] Pei, H., Zhang, J., Sun, Z. A computer simulation study on deposition patterns of cyclic diblock copolymer solution nanodroplets: influence of polymer length and concentration. *Chem. Res. Chin. Univ.,* **41** (1) (2025), 21–32.

[10] de Gennes, P. G. Wetting: statics and dynamics. *Rev. Mod. Phys.,* **57** (3) (1985), 827–863.

[11] Yan, C., Kim, K.-S., Lee, S.-K., et al. Mechanical and environmental stability of polymer thin-film-coated graphene. *ACS Nano,* **6** (3) (2012), 2096–2103.

[12] Pont, S., Foglia, F., Higgins, A. M., et al. Stability of polymer:PCBM thin films under competitive illumination and thermal stress. *Adv. Funct. Mater,* **28** (40) (2018), 1802520.

[13] Barnes, K. A., Karim, A., Douglas, J. F., et al. Suppression of dewetting in nanoparticle-filled polymer films. *Macromolecules,* **33** (11) (2000), 4177–4184.

[14] Sharma, S., Rafailovich, M. H., Peiffer, D., et al. Control of dewetting dynamics by adding nanoparticle fillers. *Nano Lett.,* **1** (10) (2001), 511–514.

[15] Krishnan, R. S., Mackay, M. E., Hawker, C. J., et al. Influence of molecular architecture on the dewetting of thin polystyrene films. *Langmuir,* **21** (2005), 5770–5776.

[16] Holmes, M. A., Mackay, M. E., Giunta, R. K. Nanoparticles for dewetting suppression of thin polymer films used in chemical sensors. *J. Nanopart. Res,* **9** (5) (2006), 753–763.

[17] Krishnan, R. S., Mackay, M. E., Duxbury, P. M., et al. Improved polymer thin-film wetting behavior through nanoparticle segregation to interfaces. *J. Phys.: Condens. Matter,* **19** (35) (2007).

[18] Mukherjee, R., Das, S., Das, A., et al. Stability and dewetting of metal nanoparticle filled thin polymer films control of instability length scale and dynamics. *ACS Nano,* **4** (7) (2010), 3709–3724.

[19] Roy, S., Bandyopadhyay, D., Karim, A., et al. Interplay of substrate surface energy and nanoparticle concentration in suppressing polymer thin film dewetting. *Macromolecules,* **48** (2) (2015), 373–382.

[20] Das, A., Dey, A. B., Manna, G., et al. Nanoparticle-mediated stabilization of a thin polymer bilayer. *Macromolecules,* **55** (5) (2022), 1657–1668.

[21] Gersappe, H. L. a. D. Dewetting dynamics of nanofilled polymer thin films. *Macromolecules,* **37** (15) (2004), pp. 5792–5799.

[22] Kropka, J. M., Green, P. F., Sumpter, V. G. S. Local polymer dynamics in polymer−C60 mixtures. *Nano Lett,* **8** (4) (2008), 1061–1065.

[23] Qian, Z., Shi, R., Lu, Z.-Y., et al. Horizontal to perpendicular transition of lamellar and cylinder phases in block copolymer films induced by interface segregation of single-chain

nanoparticles during solvent evaporation. *J. Chem. Phys.,* **159** (12) (2023), 124901.

[24] Qian, Z., Zhu, Y.-L., Lu, Z.-Y., et al. Unexpected solvent effect leading to interface segregation of single-chain nanoparticles in all-polymer nanocomposite films upon solvent evaporation. *Macromolecules,* **56** (5) (2023), 2175–2182.

[25] Kremer, K., Grest, G. S. Dynamics of entangled linear polymer melts: a molecular-dynamics simulation. *J. Chem. Phys.* **92** (8) (1990), pp. 5057–5086.

[26] Lorentz, H. A. Ueber die Anwendung des Satzes vom Virial in der kinetischen Theorie der Gase. *Ann. Phys.,* **248** (1) (1881), 127–136.

[27] Berthelot, D. Sur le mélange des gaz. *Compt. Rendus,* **126** (3) (1898), 1703–1855.

[28] Statt, A., Howard, M. P., Panagiotopoulos, A. Z. Solvent quality influences surface structure of glassy polymer thin films after evaporation. *J. Chem. Phys.,* **147** (18) (2017), 184901.

[29] Zhu, Y. L., Liu, H., Li, Z. W., et al. GALAMOST: GPU-accelerated large-scale molecular simulation toolkit. *J. Comput. Chem.,* **34** (25) (2013), 2197–2211.

[30] Khalkhali, M., Kazemi, N., Zhang, H., et al. Wetting at the nanoscale: a molecular dynamics study. *J. Chem. Phys.,* **146** (11) (2017), 114704.

[31] Barber, C. B., Dobkin, D. P., Huhdanpaa, H. The quickhull algorithm for convex hulls. *ACM Trans. Math. Software,* **22** (4) (1996), 469–483.